IMAGING WITH CADMIUM ZINC TELLURIDE DETECTOR

Arun G (TIFR), Dr Dipankar Bhattacharya(RRI) and Dr A R Rao(TIFR)

May 25, 2004

Abstract

This report is a description of the Imaging Software that is developed to produce the response of the CZT camera after reconstruction of the sky image for source at different angles of incidence. It gives an account of the software developed for the case where the gap between the detector plane and the collimator is considered to be equal to ten centimeters due to the Dummy housing in between the collimator and the detector plane. The report describes the software written to simulate sources at various angles of incidence in the field of view (FOV) of one quadrant (sixteen 4×4 basic units) of the CZT camera. Also the algorithm used to reconstruct the raw sky image of simulated source which is eventually used in the Iterative Removal Of Sources (IROS). IROS is a PSF removal procedure used to determine source positions from the reconstructed sky image. The report also describes the generation of the PSFs for all the possible angles of incidence in the FOV.

Contents

1 INTRODUCTION **2**

1.1 2-Dimensional Camera 2

1.1.1 Preview 2

1.1.2 Camera Dimension Specification and Representation 2

1.2 Simulation 3

1.2.1 High Energy Simulations 3

1.2.2 Low Energy Simulations 4

1.3 Image Reconstruction 5

1.3.1 High Energy Case 5

1.3.2 Low Energy case 10

1.4 Point Spread Function 11

1.4.1 High energy PSF's 11

1.4.2 Low energy PSF's 12

1.5 Iterative Removal Of Sources (IROS) 13

1.6 RESULTS 15

1.6.1 High energy case 15

1.6.2 Low Energy Case 18

Chapter 1

INTRODUCTION

1.1 2-Dimensional Camera

1.1.1 Preview

A previous report titled "Coded Aperture Mask and Collimator for the CZT Detector Array of ASTROSAT" by "Sushila R Mishra, Dr A R Rao and Dr Dipankar Bhattacharya" Nov 2003. describes some technical details of the Mask Pattern generation and the selection of the appropriate test mask patterns for the CZT Camera. The mask patterns are generated using eighth order polynomial which are linearly wrapped to obtain the mask patterns. From the considerations of the figure of merit calculations we choose to test the mask patterns LWrap8_m8.dat and LWrap1_m8.dat for the imaging software. The details of the Figure of merit calculations are included in the Report by Sushila R, Dr Dipankar B and Dr A R Rao dated March 10 2004. The Imaging Software developed is a two step process. The first step in the process is to accumulation of the spatially coded detector data. This is then followed by a reconstruction of the observed part of the sky. The process of the imaging software developed has been adopted from the PhD thesis *A Coded-Mask Imager As Monitor Of Galactic X-Ray Sources* by Johannes Joseph Marie in 't Zand, Utrecht University, 1992.

1.1.2 Camera Dimension Specification and Representation

The CZT array is a 32 $\times$ 32 element which is divided into 4 quadrants of 16 $\times$ 16 size . Each quadrant is made of sixteen, 4 $\times$ 4 units . The software is demonstrated for a quadrant of the CZT array.

A 4 $\times$ 4 basic unit of the detector is further subdivided into 256 pixels each of size 2.5mm $\times$ 2.5mm. This basic unit is replicated as a 4 $\times$ 4 matrix to obtain the detector of the whole Quadrant. While constructing the whole detector plane we maintain a gap of one pixel between the basic units . Hence we need a 67 $\times$ 67 array (4 * 16 +3 = 67) to represent the detector of a quadrant.

The mask pattern generated is also a similar unit.The two mask patterns chosen are used to test the software to determine their Imaging capabilities. Each pattern is a 16 $\times$ 16 array of open and closed elements generated as a result of the Linear wrapping. Each such basic pattern is replicated to form the whole quadrant of the CZT array. The inter unit distance is equal to one pixel size and hence we place a closed element in these places by which we obtain a 67 $\times$ 67 array to represent a whole quadrant of the mask plane of the CZT array.

Collimator Description

The Collimator unit for the high energy is made of Tantalum sheet of width 0.1mm which is sandwiched between 0.2mm aluminum sheets. The field of view of the high energy collimator's is 6° × 6°. Each high energy collimator's is divided into 8 units for low energy collimation. They are either divided into parallel or perpendicular sub-units as shown in figure 1.1. Aluminum sheets of thickness 0.1mm are used a low energy collimator's.Each sub unit is a 1cm × 2cm ,4 × 8 (32 pixel) unit and has a Field of View 2.29° × 1.15°.

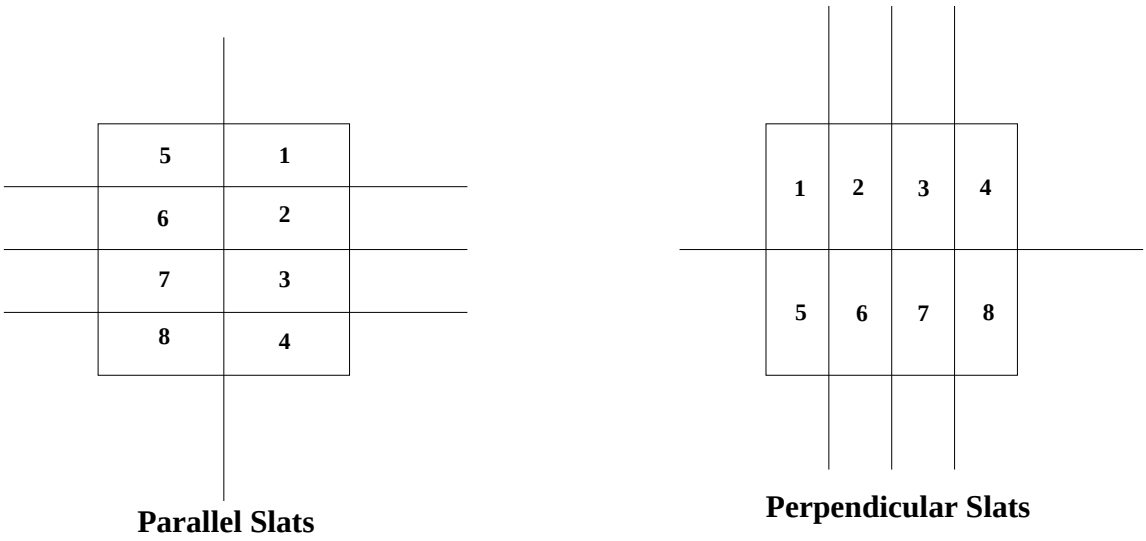

Figure 1.1: Collimator slat arrangement

From the figure of merit calculations for the low energy case we find that the parallel case yields better results and hence is chosen in the simulation and the reconstruction process.

1.2 Simulation

The imaging software is a two step procedure. the first step is to accumulate specially coded detector data due to a source in the field of view using the codded aperture mask. In this section we describe the procedure separately for the High energy and the Low energy case. Simulations have been carried out using both the mask patterns which are chosen to test their Imaging capabilities.

1.2.1 High Energy Simulations

The simulation software generates the spatially coded detector data for the whole quadrant of the CZT detector array. At the end of the simulation one obtains the 67 × 67 detector array for a user specified source position in the field of view. Monte Carlo Simulation technique is employed to simulate a large number of photons in the field of view of the CZT detector array. A source at some sky element (k,m) casts a shadow of a portion of the mask on the detector. This portion and the location of the shadow on the detector depends on the sky element (k,m). To facilitate the simulation we know that the collimator's run along the first 400mm from the mask plate and then there is no collimation in the dummy housing which is placed between the Collimator unit and the detectors. A virtual detector is assumed to be present art a distance of 100mm from the detector , this virtual detector

ensures a collimated response. The photon position is recorded on the virtual detector and is allowed to pass through to fall on the actual detector with out ant collimation.

The mask pattern and the virtual detector units are similar to each other and are divided into 16 4×4 units due to the high energy collimator's. Each such basic unit is represented by a unique number in both the mask plane and the virtual detector called the unit number.

In each step of the simulation a random position for the photon is simulated and the position at which it falls on the mask plate is recorded. The unit number on the mask plate is calculated and recorded. If the mask pattern has a closed element at the strike position the photon is not allowed to pass through and is rejected. If the mask pattern has a open element at the strike position it is allowed to pass through the mask plane. For every such photon the position at which the photon strikes the virtual detector is then calculated. The unit number of the virtual detector is then calculated and matched with the unit number on the mask plate. If the two values match then the photon is considered to have passed thought he collimator's and hit the virtual detector else the photon generated has hit the walls of the collimator and hence has to be rejected. If the unit numbers match the photon is then allowed to fall on the detector and the position of strike on the detector plate is calculated. The detector position is then converted to the pixel value and the bin count in that pixel of the detector plane is incremented. At every stage from the mask plane to the detector plane if the position of the strike of the photon is outside the dimensions of the CZT array it is rejected. Also in the detector plane if the pixel number calculated corresponds to the gap between the basic units it is not recorded as there is no detector in these positions.

The process is repeated for a user specified number of photons. At the end of the simulation one obtains the spatially coded detector data for a specified source position.

1.2.2 Low Energy Simulations

The simulation process for the low energy is the same as described for the case of high energy simulations. But to facilitate the low energy collimation the positions at which the aluminum sheets are present are calculated and recorded. At the mask plane stage if the simulated position falls on the aluminum sheets they are rejected. Further the basic unit numbers in the mask plane are unique to the low energy collimator's and there are a total of 128 unique numbers on the mask and the virtual detector planes. Only if the mask plane unit numbers match with the virtual detector the photon is allowed to pass to the detector plane else it is considered to have hit the walls of the low energy collimator's and are hence rejected.

At the end of the simulations one obtains the detector array of size 67×67 for both the High energy and the low energy calculations. From this array we extract out 16×16 units to reconstruct sky image separately for the high energy case and from the resulting array of low energy simulations we extract 4×8 sub units and reconstruct for low energy separately . The procedure to reconstruct the sky image from the simulated and extracted data is described in the following section.

1.3 Image Reconstruction

1.3.1 High Energy Case

The sky is modeled as discrete sky elements. From one sky element to the next, the shadow of the mask pattern produced by a source at that sky element moves by one detector bin. Given a 2-D 16 × 16 unit = 256 bins, a total of 1024 sky elements can be realized on the detector array.The Expression used to generate these sky elements in the terms of the detector array is shown below.

Detector Array

Let the detector bin counts be $\{b_{0,0},\ b_{0,1}, \ldots,\ b_{15,15}\}$, Corresponding to each sky element (k,m) detector vectors $D^{k,m}$ can be listed as shown below.

$$
\begin{aligned}
D^{0,0} &= \{b_{15,15}\},\\
D^{0,1} &= \{b_{15,14},\ b_{15,15}\},\\
D^{0,2} &= \{b_{15,13},\ b_{15,14},\ b_{15,15}\},\\
&\ \ \vdots \qquad\qquad\qquad\qquad \vdots\\
&\ \ \vdots \qquad\qquad\qquad\qquad \vdots
\end{aligned}
$$

$$
D^{15,15} = \left\{ \begin{array}{ccccc}
b_{0,0}, & b_{0,1}, & \ldots\ldots\ldots\ldots, & b_{0,14}, & b_{0,15}\\
\vdots & & & \vdots & \\
\vdots & & & \vdots & \\
b_{15,0}, & b_{15,1}, & \ldots\ldots\ldots\ldots, & b_{15,14}, & b_{15,15}
\end{array} \right\}
$$

$$
D^{16,16} = \left\{ \begin{array}{ccccc}
b_{0,0}, & b_{0,1}, & \ldots\ldots\ldots\ldots, & b_{0,14}, & b_{0,15}\\
\vdots & & & \vdots & \\
\vdots & & & \vdots & \\
b_{15,0}, & b_{15,1}, & \ldots\ldots\ldots\ldots, & b_{15,14}, & b_{15,15}
\end{array} \right\}
$$

$$
\begin{aligned}
&\ \ \vdots \qquad\qquad\qquad\qquad \vdots\\
&\ \ \vdots \qquad\qquad\qquad\qquad \vdots\\
D^{31,30} &= \{b_{0,0},\ b_{0,1}\},\\
D^{31,31} &= \{b_{0,0}\}.
\end{aligned}
$$

The formula that is used to obtain the detector array pattern is listed below.

$$
d_{i,j}^{k,m} = \left\{ \begin{array}{lcll}
b_{(k_{max}-i),(m_{max}-j)} & ; & 0 \le (k,m) \le 15 & ,\\
 & & (k,m) \le (i,j) \le 0 & ,\\
 & & k_{max} = m_{max} = 16 & .\\
 & & & \\
b_{i,j} & ; & k = m = 16 & ,\\
 & & 0 \le (i,j) \le (k,m) & .\\
 & & & \\
b_{(k_{max}-i),(m_{max}-j)} & ; & 17 \le (k,m) \le 31 & ,\\
 & & (k,m) \le (i,j) \le 31 & ,\\
 & & k_{max} = m_{max} = 31 & .
\end{array} \right.
$$

These vectors describe the part of the detector that is exposed for any specific sky position. Similarly mask pattern representations for specific sky elements can be realized. The following subsection describes the procedure followed to obtain the mask pattern representation of the sky plane.

Physical Mask Aperture Function

Let the mask pattern be represented as $\{a_{0,0},\ a_{0,1}, \ldots,\ a_{15,15}\}$, Corresponding to each sky element (k,m) mask element vectors $C^{k,m}$ can be listed as shown below. These mask element vectors represent the part of the sky which illuminates the mask pattern. Different sky elements cast different parts of the mask pattern on the detector. We hence have a total of 1024 patterns that can be obtained to represent the different parts of the sky , All such combinations of the sky that can be represented by the mask elements are listed below.

$$
\begin{aligned}
C^{0,0} &= \{a_{0,0}\},\\
C^{0,1} &= \{a_{0,0},\ a_{0,1}\},\\
&\vdots \qquad\qquad\qquad\qquad\qquad\qquad\qquad\qquad \vdots\\
&\vdots \qquad\qquad\qquad\qquad\qquad\qquad\qquad\qquad \vdots\\
C^{15,15} &= \left\{ \begin{array}{ccccc} a_{0,0}, & a_{0,1}, & \ldots\ldots\ldots\ldots, & a_{0,14}, & a_{0,15} \\ \vdots & & & \vdots & \\ \vdots & & & \vdots & \\ a_{15,0}, & a_{15,1}, & \ldots\ldots\ldots\ldots, & a_{15,14}, & a_{15,15} \end{array} \right\}\\
C^{16,16} &= \left\{ \begin{array}{ccccc} a_{0,0}, & a_{0,1}, & \ldots\ldots\ldots\ldots, & a_{0,14}, & a_{0,15} \\ \vdots & & & \vdots & \\ \vdots & & & \vdots & \\ a_{15,0}, & a_{15,1}, & \ldots\ldots\ldots\ldots, & a_{15,14}, & a_{15,15} \end{array} \right\}\\
&\vdots \qquad\qquad\qquad\qquad\qquad\qquad\qquad\qquad \vdots\\
&\vdots \qquad\qquad\qquad\qquad\qquad\qquad\qquad\qquad \vdots\\
C^{31,30} &= \{a_{15,14},\ a_{15,15}\},\\
C^{31,31} &= \{a_{15,15}\},
\end{aligned}
$$

The formula that is used to obtain the Mask array pattern is listed below.

$$
c_{i,j}^{k,m} = \left\{ \begin{array}{lcll} a_{(k_{max}-i),(m_{max}-j)} & ; & 0 \le (k,m) \le 15 & , \\ & & 0 \le (i,j) \le k,m & , \\ & & k_{max} = m_{max} = 16 & . \\ & & & \\ b_{i,j} & ; & k = m = 16 & , \\ & & 0 \le (i,j) \le (k,m) & . \\ & & & \\ b_{(k_{max}-i),(m_{max}-j)} & ; & 17 \le (k,m) \le 31 & , \\ & & (k,m) \le (i,j) \le 31 & , \\ & & k_{max} = m_{max} = 31 & . \end{array} \right.
$$

The number of open and closed mask elements in the Physical mask pattern is calculated and stored in files for use in the reconstruction process.

Step 2: Cross Correlation

With the above definition, we are now ready to discuss the basic steps involved in the cross-correlation procedure. While constructing the sky image, this procedure also accomplishes the subtraction of the mean background level. The following three step procedure undertaken during the cross-correlation achieves this purpose:

1. The *open* or *source* component of cross-correlation, $r_k[o]$, with $c_{i,j}^{k,m}$ and $d_{i,j}^{k,m}$ is computed as follows:

$$r_{k,m}[o] = \sum_{i,j \in D^{k,m}} c_{i,j}^{k,m} d_{i,j}^{k,m} \qquad \begin{cases} \forall & 0 \le k \le (2 \times N) - 1 \\ \forall & 0 \le m \le (2 \times N) - 1 \\ \forall & 0 \le i \le n_k - 1 \\ \forall & 0 \le j \le n_k - 1 \end{cases}$$

$r_{k,m}[o]$ has the information about sources as well as the background.
N is the number of Mask Elements

2. The *closed* or *background* component of cross-correlation, $r_{k,m}[c]$, with $\bar{c}_{i,j}^{k,m}$ and $d_{i,j}^{k,m}$ is then computed. To construct $\bar{c}_{i,j}^{k,m}$ [1], the complement of the mask pattern is used; i.e. all open slits are replaced by closed ones and vice versa.

$$r_{k,m}[c] = \sum_{i,j \in D^{k,m}} \bar{c}_{i,j}^{k,m} d_{i,j}^{k,m} \qquad \begin{cases} \forall & 0 \le k \le (2 \times N) - 1 \\ \forall & 0 \le m \le (2 \times N) - 1 \\ \forall & 0 \le i \le n_k - 1 \\ \forall & 0 \le j \le n_k - 1 \end{cases}$$

This component responds to the background, and also contains a negative image of the sources.

3. The normalized *closed* component is subtracted from the normalized *open* component, consequently removing the mean background, and adding the source contributions. The result of the subtraction is the image of the sky, $r_{k,m}$.

$$\begin{aligned} r_{k,m} &= \frac{r_{k,m}[o]}{n_k[o]} - \frac{r_{k,m}[c]}{n_k[c]} \\ &= s_{k,m} + Coding\ Noise \qquad \forall \quad 0 \le k \le 2*N-1 \end{aligned}$$

where,
$n_k[o] \rightarrow$ the number of open slits in the illuminated area on the mask.
$n_k[c] \rightarrow$ the number of closed slits in that area.
$s_{k,m} \rightarrow$ flux due to the source.

If for instance, there was a source at sky element k, m, the image shows a sharp peak at k, m (i.e., $s_{k,m}$) and variable strength peaks at sky elements other than k, m and this is due to the coding noise. Sources present at sky elements different from k, m, also illuminate a part of $D^{k,m}$, and result in Coding noise.

[1] $\bar{c}_{i,j}^{k,m} = 1 - c_{i,j}^{k,m}$

Reconstruction Array

With a few algebraic manipulations, a new matrix called the Reconstruction array can be built using the mask aperture function, $c_{i,j}^{k,m}$, and open fraction $t^{k,m}$, which will simplify the computation of the sky image to a one-step process. This one step process is a correlation output of the mask aperture function with the corresponding simulated counts in the detector plane.

The open fraction of the mask pattern, $t^{k,m}$ [that is, the ratio, $\frac{n_{k,m}[o]}{n_{k,m}}$], is defined as,

$$t^{k,m} = \frac{\sum_{j=0}^{n_k-1} c_j^k}{n_k}$$

The sum of the elements of the mask aperture function, c_j^k yields the number of open mask elements in C^k, as open and closed slits are represented by 1 and 0 respectively.

The Reconstruction array, $m_{i,j}^{k,m}$ is defined as,

$$m_{i,j}^{k,m} = \frac{c_{i,j}^{k,m} - t^{k,m}}{t^{k,m} * (1 - t^{k,m}) * n_{k,m}} \quad \begin{cases} \forall & 0 \le k \le (2\times N)-1 \\ \forall & 0 \le m \le (2\times N)-1 \\ \forall & 0 \le i \le n_k-1 \\ \forall & 0 \le j \le n_k-1 \end{cases}$$

And the cross correlation between simulated source array (the result of the simulation program) and the mask aperture function yields the reconstruction array.

$$r_{k,m} = \sum_{i,j \in D^{k,m}} d_{i,j}^{k,m} m_{i,j}^{k,m} \quad \begin{cases} \forall & 0 \le k \le (2\times N)-1 \\ \forall & 0 \le m \le (2\times N)-1 \\ \forall & 0 \le i \le n_k-1 \\ \forall & 0 \le j \le n_k-1 \end{cases}$$

where,

$r_{k,m}$ $\rightarrow$ Reconstructed Sky obtained after Cross Correlation.
$d_{i,j}^{k,m}$ $\rightarrow$ Detector Array.
$m_{i,j}^{k,m}$ $\rightarrow$ Reconstruction(Mask) Array.
$D^{k,m}$ $\rightarrow$ Represents the illuminated area on the Detector ($\forall$ j).

Sharp peaks at any sky element in this reconstructed sky image indicates the possibility of the presence of a source. If, for instance, there is a source only at a sky element k, m, peaks present in all other sky elements other than k, m, is due to a combination of the coding noise and the Poisson noise . To-wards the edges, since the number of mask elements used to normalize the reconstruction array is small, the coding noise becomes significantly high. A raw reconstructed sky image for normal incidence is shown in Figure 1.1.

At the end of the reconstruction process one obtains the sky reconstructed from the simulated data. A result of reconstruction of sky for a source simulated at normal is shown below.

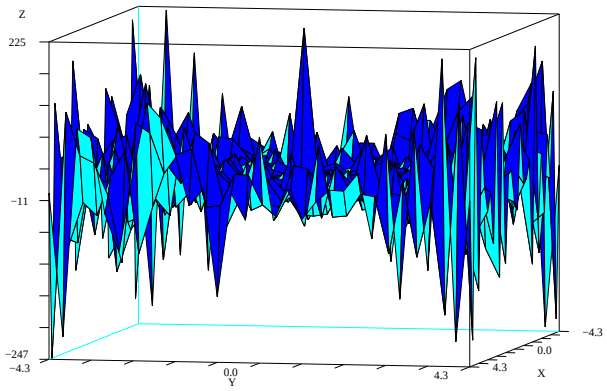

Figure 1.2: Raw image of the sky for source at normal incidence with Mask pattern one.

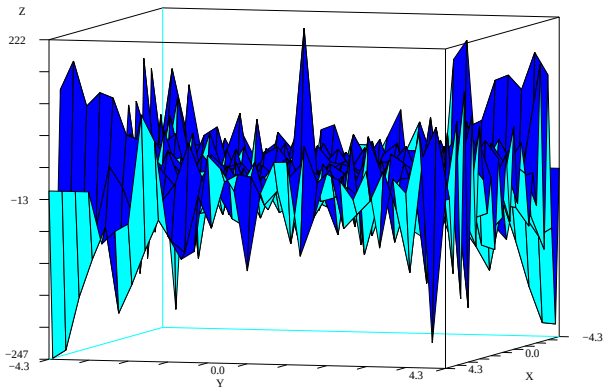

Figure 1.3: Raw image of the sky for source at normal incidence with Mask pattern eight.

1.3.2 Low Energy case

The reconstruction procedure for the Low energy case is similar to the High energy case except that the given array to the reconstruction procedure is a 2-D 4× 8 unit = 32 bins, a total of 105 sky elements can be realized on the detector array and the mask plane. A result of reconstructing the source at normal incidence is shown below.

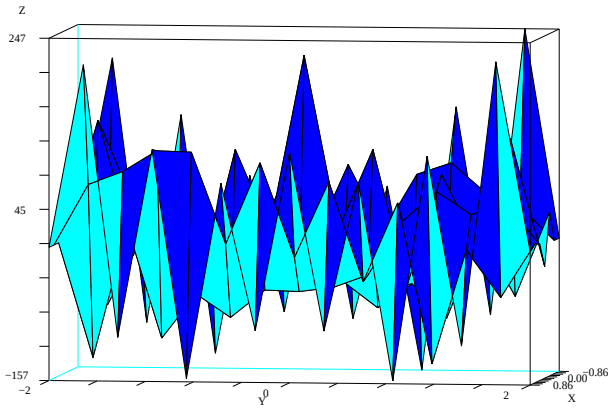

Figure 1.4: Raw image of the sky for source at normal incidence with mask pattern one.

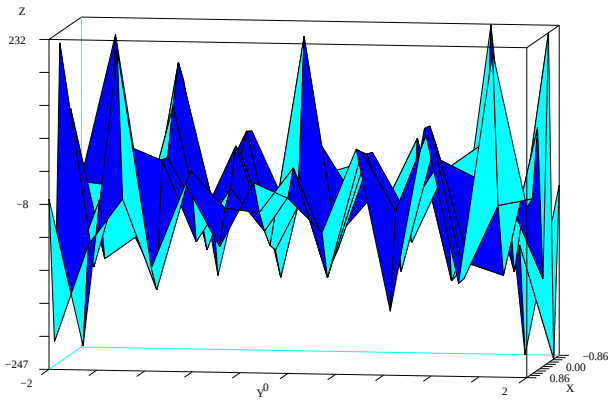

Figure 1.5: Raw image of the sky for source at normal incidence with mask pattern eight for.

1.4 Point Spread Function

1.4.1 High energy PSF's

A source at a sky location casts a unique shadow of the mask pattern. The image resulting due to this shadow is the point spread function for that sky location. Images due to sources at all sky locations in the field of view are generated and stored as point spread functions. In doing so we consider the collimator's run all along the length from the mask to the detector.

The point spread function for normal incidence is shown below.

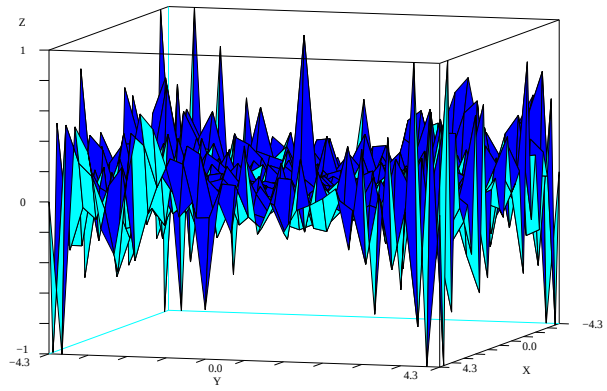

Figure 1.6: Point Spread Function for source at normal incidence for high energy case using mask pattern one

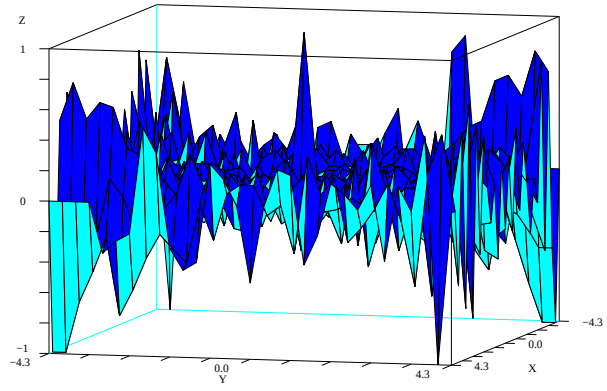

Figure 1.7: Point Spread Function of the sky for source at normal incidence using mask pattern eight.

A similar procedure is repeated for the generation of the PSF's for the low energy case using both the mask patterns.

1.4.2 Low energy PSF's

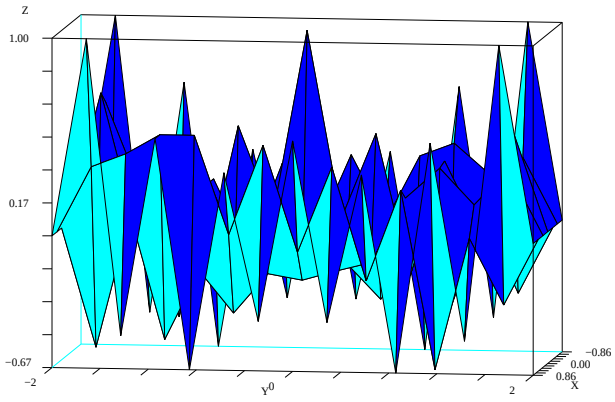

Figure 1.8: Point Spread Function of the sky for source at normal incidence using mask pattern one.

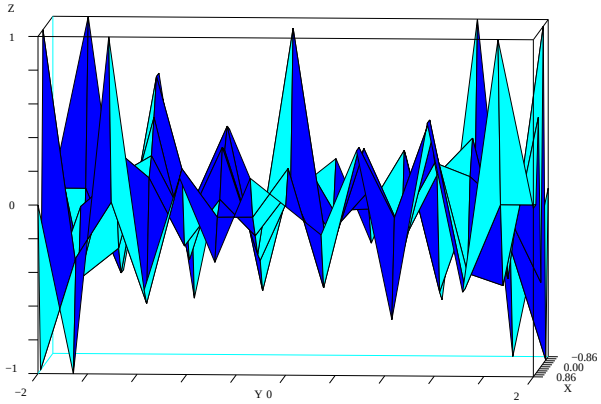

Figure 1.9: Point Spread Function of the sky for source at normal incidence using mask pattern eight.

1.5 Iterative Removal Of Sources (IROS)

The Field Of View (FOV) is divided into four concentric regions which cover the whole FOV from center to periphery. The first step in IROS is to pick the highest peak in the central region of FOV. A dummy PSF-removal is performed and it is checked if the following RMS criterion is satisfied.

$$r_b - r_a \leq \mathsf{f} \times r_b.$$

where,

$r_b \rightarrow$ RMS value of the image Before PSF-Removal.

$r_a \rightarrow$ RMS value After PSF-Removal.

f is the expected fractional improvement in RMS.

If the above RMS criterion is satisfied we store the peak picked as a candidate-source. Then the next highest peak in the central region of FOV is identified and subjected to the above RMS criterion. The procedure is continued until a peak picked does not satisfy the above RMS criterion. The candidate-source with the maximum RMS difference is chosen as the valid source which is a iterative step. If there are no candidate-sources picked in the central region of FOV the region in the FOV is expanded and checked for candidate-sources.

In every step of iteration one valid source is picked from a list of many probables (candidates). After removing every source, it is checked if some residual (either positive or negative) has cropped up in any of the *already declared* source locations. If any such residual was found, it is modeled and removed without considering the criterion of RMS improvement. The iteration is stopped when, either there is **no** candidate left in the entire FOV which can improve the RMS value beyond the specified limit, or if at all there are candidate peaks, all of them are *first-time-negative-peaks*. At the end of iteration a detailed list of all the valid sources picked are added to the final residue to generate the image of the sky. The final image obtained at the end of the iteration, will solely be due to the Poisson noise, which cannot be modeled and removed. One has to note that we only model and remove the coding noise.

The result of IROS for the source simulated at normal incidence for high energy is shown in figure 1.10. The threshold limits given to generate the output is 0.0001.

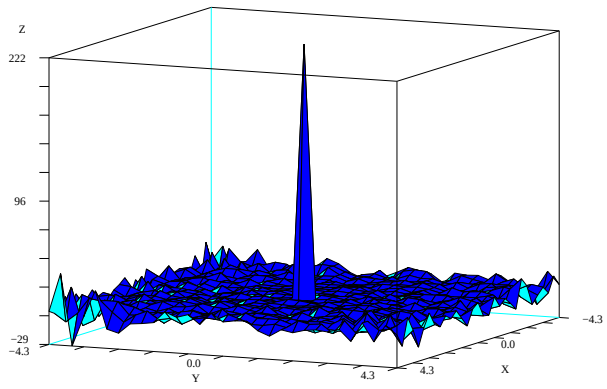

Figure 1.10: Resulting Image of the Sky after IROS, source simulated at normal incidence.

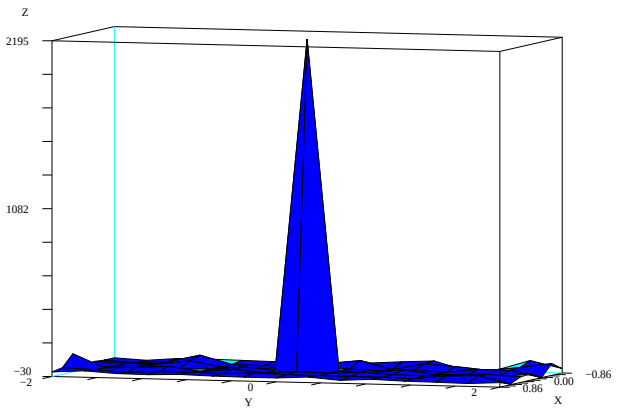

Figure 1.11: Resulting Image of the Sky after IROS, source simulated at normal incidence

The result of IROS for the source simulated at normal incidence for low energy is shown in figure 1.11. The threshold level specified for the rms criterion is 0.0001.

1.6 RESULTS

In this section we present the results due to the extension of the height using the dummy housing and the degradation of the images due to the effects of the dummy housing. The degradation is due to the seepage of the photons from the adjacent 4×4 unit. We expect the least amount of degradation at the units which are at the edges as they have only a few neighboring units and the image to be degraded more at the units in the centers as they have many neighboring units contributing to the seepage. In all the cases the imaging algorithm is tested only for a single source simulated in the field of view.

1.6.1 High energy case

A few test cases of the simulations at various angles of incidence are shown for a comparison in this section. The results of the IROS clearly show the degradation of the image due to the raising of the collimator by a height of 100 millimeters.

To show the degradation of the image we compare the results of the images due the the simulation of the source with collimator's of height 500mm with those of the images with the dummy housing in between the collimator and the detector plane where the height of the collimator is 400mm. The figure 1.12 is the result of the IROS for the simulation with collimator height of 500mm. Figure 1.13 is the result of the source simulated at normal angle of incidence and the reconstruction is carried out for a edge unit using mask pattern one and eight respectively with the collimator height of 400mm. Figure 1.14 is the result of the reconstruction at the central unit with collimator height of 400mm. For normal incidence there is no seepage and hence we expect no degradation of the image and the results show no degradation as expected.

But if we choose to reconstruct the source at off-normal incidence the degradation occurs due to the seepage of the photons from the neighboring units and the results shown below clearly show the degradation. Further the reconstruction for the sky for the unit at a edge shows lesser degradation than that for the unit at the center.

Figure 1.15 is the result of the simulation carried out with the collimator of height 500 mm.We compare this with the results of the simulation carried out with the collimator of height 400 mm. Figure 1.16 are images resulting from the reconstruction of the data extracted at the edge unit. Figure 1.17are the image resulting from the reconstruction of the data extracted at the central unit.

From the results we clearly see the degradation of the image due to the raising for the collimator's by 100mm.And the degradation is more in the case of the central units because there is more seepage of electrons in the central units than that in the case of edge units.

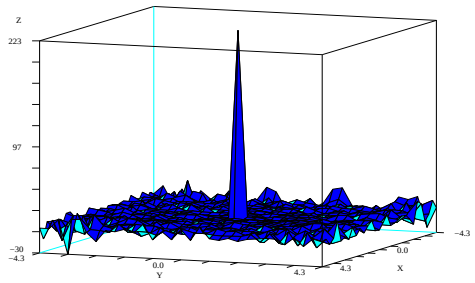

Figure 1.12: Image of sky for source at normal angle of incidence with collimator running for 500 mm.

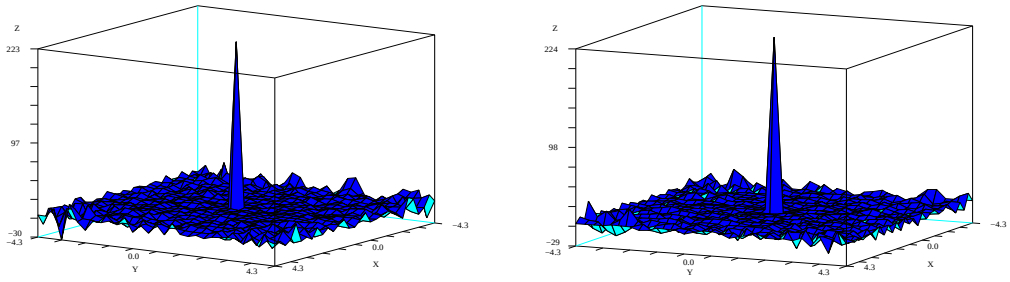

Figure 1.13: Image of sky at the edge unit for source at normal angle of incidence for pattern one and pattern eight with collimator height of 400 mm.

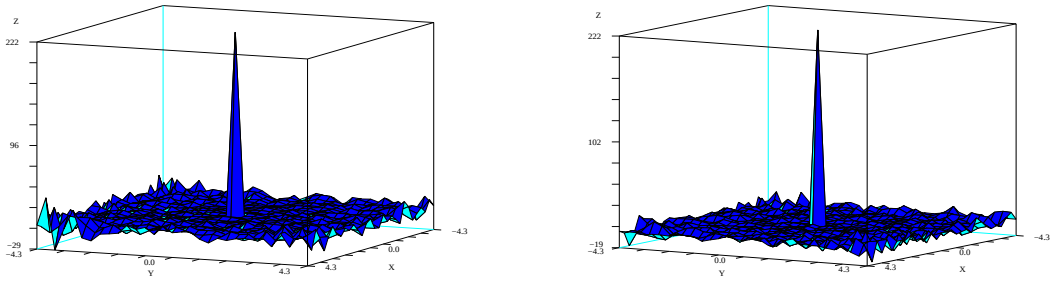

Figure 1.14: Image of sky at the central unit for source at normal angle of incidence. for pattern one and pattern eight with collimator height of 400 mm.

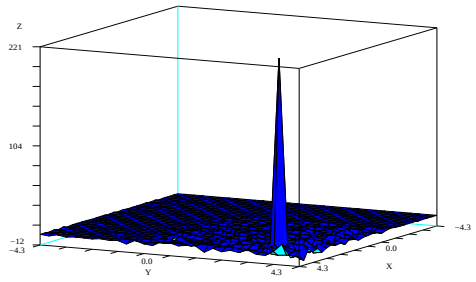

Figure 1.15: Image of sky at the central unit for source at off-normal angle of incidence with collimator running for 500 mm.

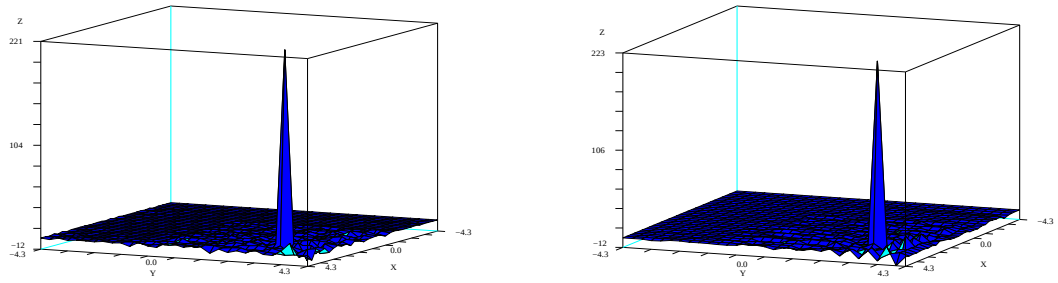

Figure 1.16: Image of sky at the edge unit for source at off-normal angle of incidence with collimator height of 400 mm.

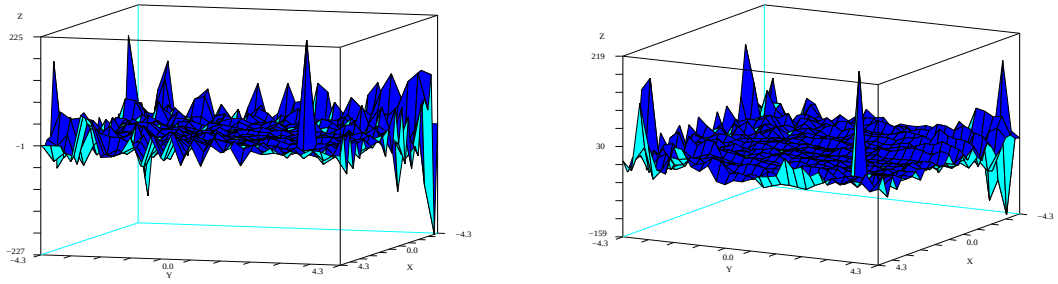

Figure 1.17: Image of sky at the central unit for source at off-normal angle of incidence with collimator height of 400 mm.

1.6.2 Low Energy Case

A similar comparison as described in the high energy case is also done for the low energy case.

Figures 1.18 is the result considering the collimator height of 500mm. figure 1.19 are the results of the sources simulated at normal angle of incidence using mask pattern one and eight respectively with the dummy housing in between the collimator unit and the detector plane. Clearly there is no degradation of the images for sources at normal angle of incidence as expected. But if a off normal angle of incidence is used to simulate

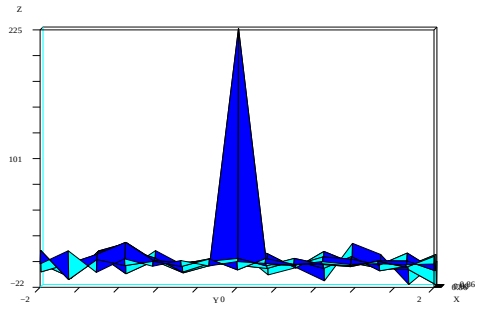

Figure 1.18: Image of sky at normal angle of incidence with collimator running for 500 mm.

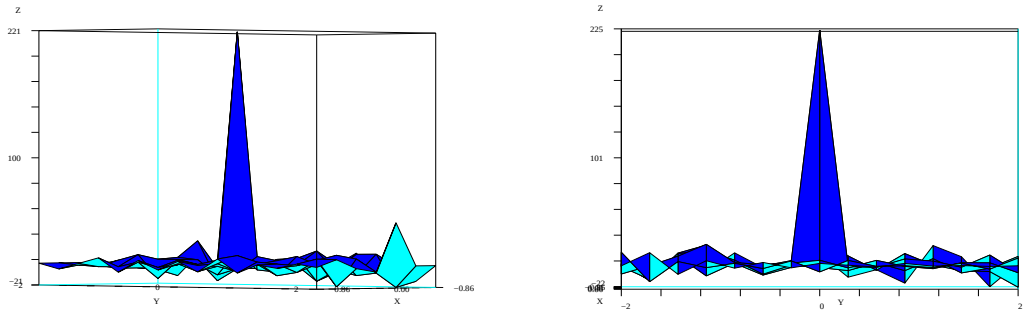

Figure 1.19: Image of sky at the edge unit for source at normal angle of incidence with collimator height of 400 mm.

the source we see the expected degradation in the image. figure 1.20 is the result with the collimator running for 500 mm .figure 1.21 are results of the source simulated at off-normal angle of incidence and the reconstruction is carried out for the edge unit. There is only a little or no degradation of the image at the edges and Figure **??** is the resulting degradation at the central unit. The results clearly shows less degradation

A similar result using the mask pattern eight is shown in figure 1.22 and figure 1.22

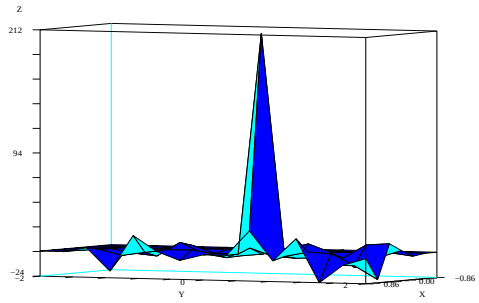

Figure 1.20: Image of sky at off-normal angle of incidence with collimator running for 500 mm for pattern one.

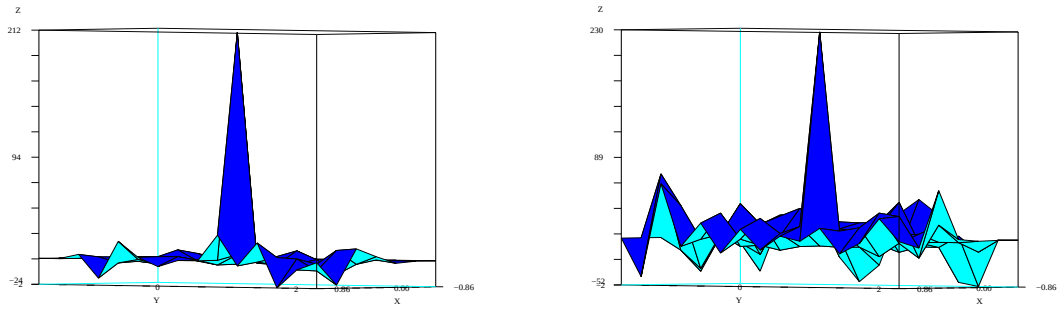

Figure 1.21: Image of sky at the edge and central unit for source at off-normal angle of incidence with dummy housing considered for pattern one with collimator height of 400 mm.

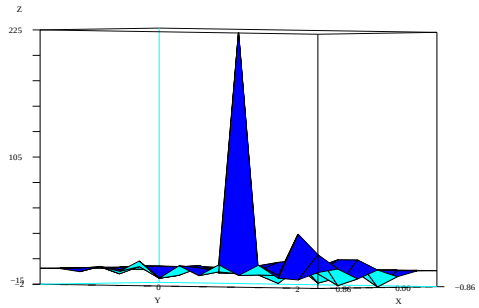

Figure 1.22: Image of sky at off-normal angle of incidence for pattern eight with collimator height of 500 mm.

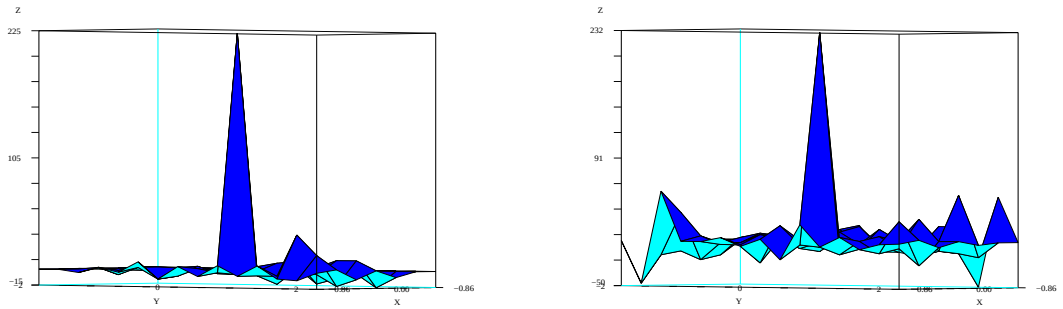

Figure 1.23: Image of sky at the edge unit and central units for source at off-normal angle of incidence